Magnetic structure of paramagnetic MnO

Joseph A. M. Paddison,[1,2,3,4] Matthias J. Gutmann,[2] J. Ross Stewart,[2] Matthew G. Tucker,[2,5,6] Martin T. Dove,[7]
David A. Keen,[2] and Andrew L. Goodwin[1,*]

[1]*Department of Chemistry, University of Oxford, Inorganic Chemistry Laboratory, South Parks Road, Oxford OX1 3QR, United Kingdom*
[2]*ISIS Facility, Rutherford Appleton Laboratory, Harwell Campus, Didcot OX11 0QX, United Kingdom*
[3]*Churchill College, University of Cambridge, Storey's Way, Cambridge CB3 0DS, United Kingdom*
[4]*School of Physics, Georgia Institute of Technology, Atlanta, Georgia 30332, USA*
[5]*Diamond Light Source, Chilton, Oxfordshire, OX11 0DE, United Kingdom*
[6]*Spallation Neutron Source, Oak Ridge National Laboratory, Oak Ridge, Tennessee 37831, USA*
[7]*School of Physics and Astronomy, Queen Mary University of London, Mile End Road, London E1 4NS, United Kingdom*

Using a combination of single-crystal neutron scattering and reverse Monte Carlo refinements, we study the magnetic structure of paramagnetic MnO at a temperature (160 K) substantially below the Curie-Weiss temperature $|\theta| \sim 550$ K. The microscopic picture we develop reveals a locally ordered domain structure that persists over distances many times larger than the correlation length implied by direct analysis of the spin-correlation function. Moreover, the directional dependence of paramagnetic spin correlations in paramagnetic MnO differs in some important respects from that of its incipient ordered antiferromagnetic state. Our results demonstrate that atomistic refinement to large three-dimensional neutron-scattering datasets is a practical approach, and have implications for the understanding of paramagnetic states in weakly frustrated systems, including high-temperature superconductors.

I. INTRODUCTION

In frustrated magnets, long-range magnetic order emerges at a temperature T_c substantially lower than the effective energy scale of magnetic interactions (i.e., the Curie-Weiss temperature $|\theta|$) [1]. A distinction is usually drawn between "weak" and "strong" frustration, associated with values of the frustration parameter $f = |\theta|/T_c$ respectively smaller or larger than 10 [2]. While the field has traditionally focused on the exotic states accessible in strongly frustrated systems [3], weak frustration nevertheless plays a key role in the magnetic behavior of a number of canonical antiferromagnets, including MnO [4]. Of particular interest is the cooperative paramagnet (PM) regime $T_c < T < |\theta|$ where magnetic interactions are still energetically relevant, yet incapable of driving long-range magnetic order. The "fluctuating spin-stripe" phases of cuprate superconductors are an ever-topical example of precisely such a state [5].

Given the importance of these canonical systems, it is perhaps surprising how little is known from an experimental viewpoint about the spin structures of cooperative PM states in weakly frustrated magnets. The assumption is usually made that local magnetic order resembles that in the incipient ordered state [6], but is confined to small domains whose size is determined by the characteristic rate of decay of the spin-correlation function [5,7]. This assumption is also implicit in conventional analysis of magnetic diffuse scattering via Lorentzian fits [8,9]. In principle, the validity of this picture

can be tested experimentally: magnetic diffuse scattering is sensitive to the three-dimensional spin correlations present in magnets—whether ordered or disordered [10,11]. When coupled with real-space refinement tools such as the reverse Monte Carlo (RMC) approach, this scattering can be used to generate experiment-driven atomic-scale models of the corresponding spin structure [12–17].

In this study, we apply this combination of diffuse scattering and RMC analysis to determine the magnetic structure of MnO within its cooperative PM regime. Our analysis includes an implementation of the RMC approach that allows direct fitting to single-crystal magnetic diffuse scattering. We find evidence of an extensive domain structure that is locally similar to the ordered antiferromagnetic (AFM) state but that also supports spin correlations forbidden by AFM order. Moreover, the domain sizes are substantially larger than suggested by direct analysis of the spin-correlation function.

Our paper is arranged as follows. We begin with a short introduction to the magnetic behavior of MnO. We then describe in turn the methods used in our study, including the new RMC implementation for single-crystal diffuse scattering, and the results of our magnetic structure investigation of paramagnetic MnO. We conclude with a brief discussion of the implications of our results for other weakly frustrated cooperative paramagnets.

Above its magnetic ordering temperature $T_N = 118$ K, MnO has the rocksalt structure, in which magnetic Mn^{2+} ions ($S = 5/2$, $L = 0$) occupy a face-centred-cubic lattice. The presence of weak frustration in MnO is indicated by a modest value of the frustration parameter $|\theta|/T_N \approx 5$ [18], which occurs because the frustrated antiferromagnetic (AFM)
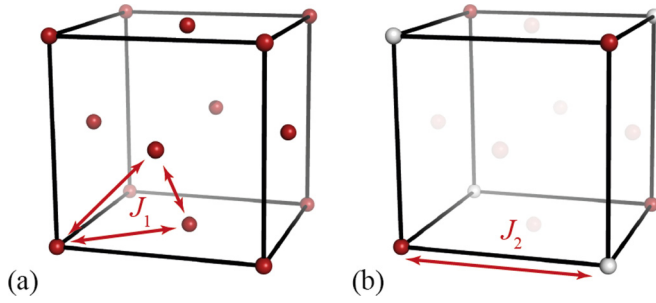
FIG. 1. (a) Nearest-neighbor AFM interactions (J_1) are frustrated on the face-centered-cubic lattice. (b) Next-nearest-neighbor AFM interactions (J_2) are not frustrated and drive checkerboard ordering of the simple cubic sublattices.

coupling between nearest neighbors is smaller than the unfrustrated next-nearest-neighbor coupling (Fig. 1) [19]. Below T_N, long-range AFM order develops with magnetic propagation vector $\mathbf{k} = [\frac{1}{2}\frac{1}{2}\frac{1}{2}]^*$ [20]. In the ordered AFM structure, spins are aligned parallel within (111) planes, and the spin direction is reversed in adjacent (111) planes [21]. The nearest-neighbor interactions within (111) planes are therefore frustrated, and a rhombohedral lattice distortion occurs in order to alleviate this frustration [22,23].

Previous neutron-scattering studies have shown that structured magnetic diffuse scattering is present above T_N (Refs. [6,10,24]) and short-range spin correlations persist to $T \gtrsim 1100$ K [13,25]. Yet, all previous measurements have been restricted to either individual reciprocal-space planes or the powder average, limiting the information content of the scattering pattern [26]. Advanced neutron-scattering instruments now allow measurement of essentially complete three-dimensional (3D) diffuse-scattering patterns [27,28], but a key problem remains: analysis of these very large datasets is usually computationally prohibitive [26]. Here, we develop an approach to allow rapid refinement of an atomic-scale model to magnetic diffuse-scattering datasets containing $>10^6$ data points. We demonstrate the success of this approach by fitting to the complete 3D magnetic diffuse-scattering pattern for MnO, allowing us to determine the relationship between PM and AFM structures.

II. METHODS

Single-crystal neutron-scattering data were collected at $T = 160$ K ($\simeq 1.4 T_N$ and $0.3|\theta|$) using the SXD diffractometer at the ISIS neutron source [27]. The sample was an approximately cylindrical crystal of average diameter 7 mm, length 24 mm, and mass 4.4 g. The data were corrected for instrumental background scattering by subtracting the scattering intensity from an empty sample holder and were normalized using the incoherent scattering from a vanadium standard. The crystal structure (space group $Fm\bar{3}m$) was refined to the nuclear Bragg intensities using the JANA software package [29], using the lattice parameter $a = 4.4344(7)$ Å obtained from SXD at $T = 160$ K. The data were binned in intervals of 0.04 reciprocal-lattice units, the $m\bar{3}m$ diffraction symmetry appropriate for MnO was applied, and nuclear Bragg peaks were removed by excising regions where the intensity exceeded
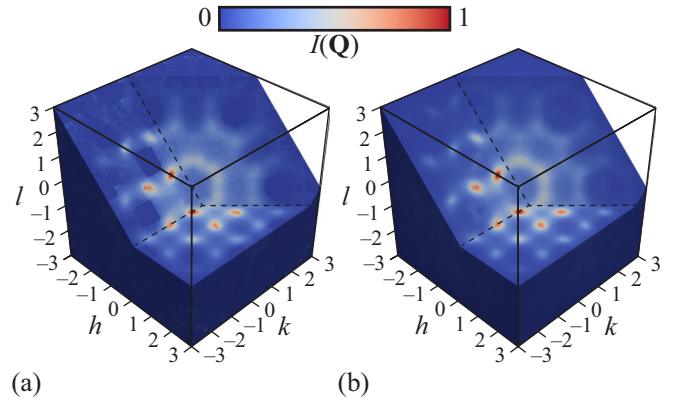
FIG. 2. (a) Experimental magnetic diffuse-scattering data for paramagnetic MnO at $T = 160$ K. Nuclear Bragg peaks have been removed from the data. (b) RMC fit to the experimental data shown in (a). In (a) and (b), sections of the $(101)^*$, $(1\bar{1}1)^*$, and $(001)^*$ reciprocal-space planes are shown. The $(001)^*$ plane is shifted by -0.5 reciprocal-lattice units along the $[001]^*$ direction in order to highlight the strongest diffuse scattering features; i.e., it is the $(h, k, -\frac{1}{2})^*$ plane.

a threshold value, plus a small surrounding volume. A 3D representation of the experimental data is shown in Fig. 2(a).

We employ reverse Monte Carlo (RMC) refinement [15,30,31] to fit spin configurations to our neutron-scattering data. In RMC refinement, a supercell of the crystallographic unit cell is generated, classical spin vectors $\mathbf{S}_i$ are assigned to each magnetic atom, and the orientations of these spins are refined to match experimental data. The approximation of spin orientations in terms of classical vectors is least severe in the case of large S, as for Mn^{2+} ($S = 5/2$). We use a cubic supercell of side length $R = 12a$ ($N = 6912$ spins) with periodic boundary conditions. Refinements are initialized with random spin orientations and are iterated to minimize the cost function

$$\chi^2 = \sum_{\mathbf{Q}} [s I_{\text{calc}}(\mathbf{Q}) + B - I_{\text{expt}}(\mathbf{Q})]^2, \quad (1)$$

where $I(\mathbf{Q})$ denotes the magnetic diffuse-scattering intensity at reciprocal-space position $\mathbf{Q}$, subscripts "calc" and "expt" denote calculated and experimental data points, s is a refined intensity scale factor, and B is a refined flat-in-$\mathbf{Q}$ term which corrects for the significant incoherent scattering from Mn [32]. Results from four separate refinements were averaged to increase the statistical accuracy. The magnetic diffuse-scattering intensity is calculated as

$$I(\mathbf{Q}) = \frac{C[g f(Q)]^2 T^2}{N} \sum_{\mathbf{G}} |\mathbf{F}(\mathbf{G})|^2 W(\mathbf{Q} - \mathbf{G}), \quad (2)$$

where $C = (\gamma_n r_0/2)^2$ is a constant, $f(Q)$ is the Mn^{2+} magnetic form factor [33], $T^2 = \exp(-U_{\text{iso}} Q^2)$ where $U_{\text{iso}} = 0.00509(9)$ Å^2 is the isotropic atomic displacement factor for Mn, and $\mathbf{G}$ is a reciprocal-lattice vector of the RMC supercell. The magnetic structure factor

$$\mathbf{F}(\mathbf{G}) = \sum_{i=1}^{N} \mathbf{S}_i^{\perp} \exp(i\mathbf{G} \cdot \mathbf{r}_i), \quad (3)$$

where $\mathbf{S}_i^{\perp} = \mathbf{S}_i - [(\mathbf{S}_i \cdot \mathbf{G})\mathbf{G}]/G^2$ is the projection of the spin located at $\mathbf{r}_i$ perpendicular to $\mathbf{G}$. We use Lanczos resampling [34] to interpolate values of $|\mathbf{F}(\mathbf{G})|^2$ at the experimentally measured $\mathbf{Q}$ points by applying the weight function [34]

$$W(\mathbf{Q}) = \prod_{\alpha} \operatorname{sinc}(Q_{\alpha} R/2)\operatorname{sinc}(Q_{\alpha} R/2m), \qquad (4)$$

where $\alpha \in \{x, y, z\}$ denotes Cartesian components, m is an integer determining the interpolation accuracy, and $W(\mathbf{Q}) \equiv 0$ outside the range $-m < Q_{\alpha}R/2\pi < m$. We take $m = 4$, which allows the spin correlations to be calculated with $\pm 1\%$ accuracy for $0 \leqslant r_{\alpha} \leqslant 12$ Å. Importantly, the computational cost of updating $I(\mathbf{Q})$ after a single spin rotation scales approximately linearly with the number of $\mathbf{Q}$ points, and avoids redundant calculations necessary in current approaches where the supercell is divided into multiple "subboxes" [35,36]. Our approach nevertheless preserves an important feature of the subbox approach, which is gradually to de-emphasize correlations at longer distances (here, $r > 12$ Å) that would add to the noise in the calculated scattering pattern [35,36]. Our approach therefore allows rapid refinement of atomic-scale models to very large datasets; e.g., each of our refinements to $\approx 1.5 \times 10^6$ $\mathbf{Q}$ points took ≈ 27 h of CPU time on a single core of an Intel Xeon processor. We expect our RMC refinement program to be applicable to 3D magnetic diffuse-scattering data from a wide range of systems [37].

III. RESULTS

The experimental neutron-scattering data shown in Fig. 2(a) show highly structured magnetic diffuse scattering, indicating a magnetic state with significant correlations. Diffuse peaks are observed at $\mathbf{G} \pm [\frac{1}{2}\frac{1}{2}\frac{1}{2}]^*$ and symmetry-related positions, and are elongated along specific $\langle 111 \rangle^*$ directions [Fig. 2(a)]. This selective elongation suggests that a description of the diffuse scattering in terms of a product of Lorentzian line shapes is not appropriate, because such a description would require that every diffuse peak has the point symmetry of the lattice [8,9]. An early study [6] reported that the diffuse $[\frac{1}{2}\frac{1}{2}\frac{1}{2}]^*$ peak was split into a central peak and two satellites in the paramagnetic phase, a result that was not reproduced by a recent single-crystal study [24]; our data also show no evidence for such a splitting. The RMC fit to neutron-scattering data is shown in Fig. 2(b). Excellent agreement is achieved with the experimental data, with the weighted-profile R factor $R_{\mathrm{wp}} \approx 8.3\%$. Essentially identical fits were obtained for refinements initialized from different random starting configurations, demonstrating the reproducibility of the results (the value of R_{wp} was between 8.27% and 8.30% for the four such refinements we performed). This result shows that an atomistic configuration has been refined to a full 3D $I(\mathbf{Q})$ data set.

The spin Hamiltonian of MnO has previously been characterized using inelastic neutron-scattering measurements in the ordered AFM phase [19] and diffuse-scattering measurements of the $(110)^*$ plane in the PM phase [24]. A Heisenberg model with AFM nearest- and next-nearest-neighbor exchange constants has been employed to describe the PM phase [24],

$$H = -J_1 \sum_{\langle i,j \rangle} \mathbf{S}_i \cdot \mathbf{S}_j - J_2 \sum_{\langle\langle i,j \rangle\rangle} \mathbf{S}_i \cdot \mathbf{S}_j, \qquad (5)$$

where $\mathbf{S}_i$ are classical vectors of magnitude $\sqrt{S(S+1)}$, and angle brackets $\langle \rangle$ and $\langle\langle \rangle\rangle$ indicate that the sum is taken over nearest-neighbor and next-nearest neighbor pairs, respectively, with each pair counted twice. A good description of the magnetic diffuse-scattering data at $T \approx 160$ K is provided by Eq. (5) with $J_1 = -3.3$ K and $J_2 = -4.6$ K, respectively [24]. As a check on our RMC refinement, we simulated this J_1-J_2 model at 160 K using direct Monte Carlo simulations. These simulations were initialized at a high temperature (1360 K) and cooled in 200-K steps to the simulation temperature of 160 K. At each temperature, the number of proposed moves per spin was chosen to be at least $10t_0$, where t_0 is the number of proposed moves per spin needed to decorrelate the system ($t_0 \approx 70$ at 160 K). Results were averaged over 16 independent configurations to improve statistics. From these simulations, we first calculate the radial correlation function of the normalized spins at 160 K,

$$\langle \mathbf{S}(0) \cdot \mathbf{S}(r) \rangle = \frac{1}{NS(S+1)} \sum_{i=1}^{N} \sum_{j=1}^{Z_i(r)} \frac{\mathbf{S}_i \cdot \mathbf{S}_j}{Z_i(r)}, \qquad (6)$$

where $Z_i(r)$ is the number of spins that coordinate a central spin i at distance r. Figure 3(a) compares the $\langle \mathbf{S}(0) \cdot \mathbf{S}(r) \rangle$ obtained from RMC refinement with the results for the J_1-J_2 model. The trend in the correlations is identical between the two calculations; quantitatively, the difference in magnitude of the next-nearest-neighbor correlation value is 7%. The spin-correlation length $\xi = 2.258(3)$ Å $\simeq a/2$ was obtained by fitting $\exp(-r/\xi)$ to $|\langle \mathbf{S}(0) \cdot \mathbf{S}(r) \rangle|$ over the set of distances for which $|\langle \mathbf{S}(0) \cdot \mathbf{S}(r) \rangle|$ is larger than at all longer distances. We will come to show that local magnetic order persists over a length scale substantially larger than ξ. The maximum value of $\langle \mathbf{S}(0) \cdot \mathbf{S}(r) \rangle$ obtained from RMC refinement was 0.1512(4) at the next-nearest-neighbor distance, which is much smaller than the maximum value of $S^2/S(S+1) \approx 0.71$ expected in an ordered state. Motivated by the evidence from γ-ray diffraction for a nonspherical distortion of the d-electron density in the PM phase [38], we also calculated the distribution of spin orientations from our RMC refinements but observed no statistically significant anisotropy in the spin orientations. This result is consistent with the observation that the magnetic dipolar interaction is mainly responsible for magnetic anisotropy in MnO [39,40], but its strength $DS^2 \approx 8$ K (Ref. [19]) is much smaller than the thermal energy at 160 K. The results from RMC refinement therefore agree closely with the J_1-J_2 Heisenberg model of PM MnO, validating the methodology of 3D RMC refinement.

Access to 3D spin configurations allows us to probe magnetic structure in more depth than given by radial spin-correlation functions alone. Our particular interest is in understanding the relationship between the PM and AFM states in MnO. The $\langle \mathbf{S}(0) \cdot \mathbf{S}(r) \rangle$ function shown in Fig. 3(a) already hints that the PM correlations do not simply resemble the AFM correlations multiplied by a decreasing function of distance. As expected from the relative magnitudes of J_1 and J_2, the strongest correlation is between next-nearest neighbors, for which AFM interactions are not frustrated. However, significant AFM correlation is present at the nearest-neighbor distance in the PM phase, whereas this radially averaged
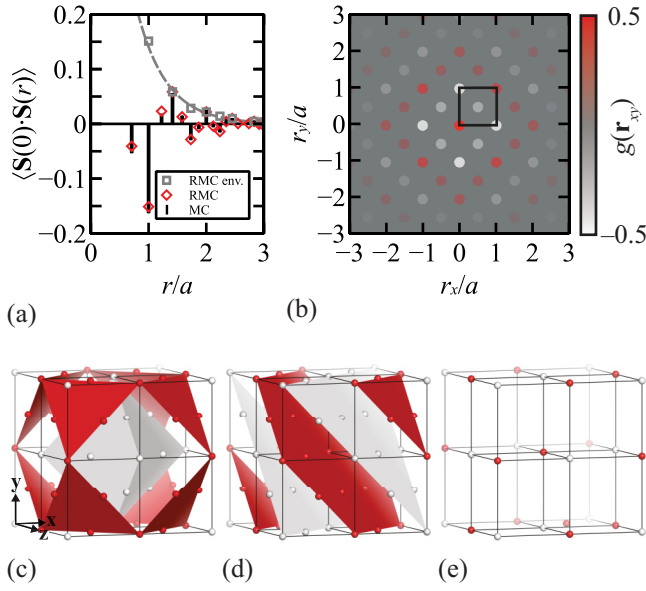
FIG. 3. (a) Radial spin-correlation function $\langle \mathbf{S}(0) \cdot \mathbf{S}(r) \rangle$ for MnO at $T = 160$ K. Black bars show results for the J_1-J_2 model described in the text and red diamonds show results from RMC refinement to single-crystal magnetic diffuse-scattering data. The dashed grey line shows the fit of an exponential envelope to the RMC $|\langle \mathbf{S}(0) \cdot \mathbf{S}(r) \rangle|$, which yields spin-correlation length $\xi = 2.258(1)$ Å. Grey squares show the $|\langle \mathbf{S}(0) \cdot \mathbf{S}(r) \rangle|$ values included in the fit. Error bars are smaller than the symbol size in the plot. (b) 3D spin-correlation function $g(\mathbf{r})$ (defined in the text) obtained from RMC refinement. The figure shows the $(xy0)$ plane (i.e., a cubic face). The crystallographic unit cell is shown as a black box. (c) Schematic representation of $g(\mathbf{r})$ for MnO in the PM phase. Red areas indicate FM correlations and grey areas AFM correlations. (d) Schematic representation of $g(\mathbf{r})$ for a single domain of the ordered low-temperature AFM structure of MnO. (e) Schematic representation of $g(\mathbf{r})$ obtained for the AFM structure with the point symmetry of the Mn site in the PM state applied.

correlation is exactly zero for the ordered AFM state. This result implies that the absence of long-range order allows frustrated nearest-neighbor interactions to be partially satisfied in the PM phase. In order to assess the influence of the frustrated geometry on the spin correlations, we consider the 3D correlation function of normalized spins, $\langle \mathbf{S}(0) \cdot \mathbf{S}(r) \rangle$. This function reveals the dependence of spin correlations on the lattice geometry, which is expected to be important in frustrated systems [41]. In order to emphasize the directional dependence of the longer-range correlations, we calculate the quantity

$$ g(\mathbf{r}) = \frac{\langle \mathbf{S}(0) \cdot \mathbf{S}(r) \rangle}{\sqrt{|\langle \mathbf{S}(0) \cdot \mathbf{S}(r) \rangle|}}. \qquad (7) $$

Figure 3(b) shows that a distinctive pattern—hidden in the radial correlation function—emerges in $g(\mathbf{r})$. The $g(\mathbf{r})$ can be described as a set of nested octahedral shells, with the sign of the spin correlations alternating between FM and AFM for successive shells as distance is increased [Fig. 3(c)]. As anticipated, this pattern extends over length scales much greater than ξ. Hence, taking each Mn atom in turn as the origin, Mn neighbors at coordinates $\mathbf{r}/a = [x, y, z]$ are (on average) ferromagnetically correlated if $x + y + z$ is even, and antiferromagnetically correlated if $x + y + z$ is odd. The sign

of $g(\mathbf{r})$ is consistent with the facts that J_1 and J_2 interactions are both AFM and the smallest number of exchange pathways which connects two Mn^{2+} ions is given by $x + y + z$.

To what extent are these local correlations related to the spin structure of the low-temperature AFM phase? The description of the PM spin-correlation function of MnO as a set of nested octahedral shells [Fig. 3(c)] is compared in Figs. 3(d) and 3(e) with, respectively, the spin-correlation function for a single domain of the AFM structure and the same correlation function with the point symmetry of the Mn site in PM MnO ($m\bar{3}m$) applied. In a single domain of the AFM structure [Fig. 3(d)], spins are ferromagnetically aligned within (111) planes and the direction of spin alignment reverses between adjacent planes [21]; hence, the PM correlations resemble the AFM structure viewed along the [111] direction. However, an average over the spin-correlation functions for symmetry-equivalent AFM domain orientations [Fig. 3(e)] cannot fully describe the PM correlations, because $g(\mathbf{r})$ vanishes for nearest-neighbor spins in this case. The RMC results [Fig. 3(b)] are intermediate between Figs. 3(c) and 3(e): the signs of the spin correlations are described by Fig. 3(c) but the magnitudes of the spin correlations are largest at the positions shown in Fig. 3(e). Consequently, an interpretation of the PM phase in terms of local AFM order explains the strongest spin correlations but is nevertheless an oversimplification because the nature of the nearest-neighbor correlations is different in PM and AFM states. These results are entirely consistent with the early theoretical studies of Refs. [42,43] based on the random-phase Green's-function approximation, and recent magnetic pair-distribution function (mPDF) analysis of powder neutron-scattering data [44].

We proceed to explore the length scale over which this modified AFM-like local order persists. In the conventional interpretation, local AFM order is characterized by one of the four symmetry-equivalent $\mathbf{k} \in \langle \frac{1}{2} \frac{1}{2} \frac{1}{2} \rangle^*$ [6,45]. It is assumed that different $\mathbf{k}$ are selected within separate regions of the crystal, so that the overall cubic symmetry of the PM phase is preserved. To look for such domain structure in the RMC spin configurations, we calculate a local version of the magnetic scattering factor that functions as a locally averaged order parameter [46],

$$ S_{\mathbf{k}}(\mathbf{r}) = \left| \sum_i w(|\mathbf{r} - \mathbf{r}_i|) \mathbf{S}_i \exp\left(i \frac{2\pi}{a} \mathbf{k} \cdot \mathbf{r}_i \right) \right|^2, \qquad (8) $$

where $\mathbf{k} \in \langle \frac{1}{2} \frac{1}{2} \frac{1}{2} \rangle^*$, $\mathbf{r}_i$ is the position of spin $\mathbf{S}_i$ within the configuration, and the continuous variable $\mathbf{r}$ denotes position within the configuration. The local averaging function $w(|\mathbf{r} - \mathbf{r}_i|)$ is chosen to be a decaying function of $|\mathbf{r} - \mathbf{r}_i|$, so that the $S_{\mathbf{k}}(\mathbf{r})$ is sensitive to local correlations [46]; we take

$$ w(|\mathbf{r} - \mathbf{r}_i|) = \exp\left(-\frac{|\mathbf{r} - \mathbf{r}_i|}{2\xi} \right). \qquad (9) $$

The physical motivation for this choice is to reflect the approximately exponential decay of $|\langle \mathbf{S}(0) \cdot \mathbf{S}(r) \rangle|$ with correlation length ξ [Fig. 3(a)]; the factor of 2 in the denominator of Eq. (9) occurs because the scattering intensity is proportional to the square of the magnetic structure factor. We assign each site as a member of domain with propagation vector $\mathbf{k}$ if $S_{\mathbf{k}}$ exceeds a threshold value, which is chosen to maximize the number of
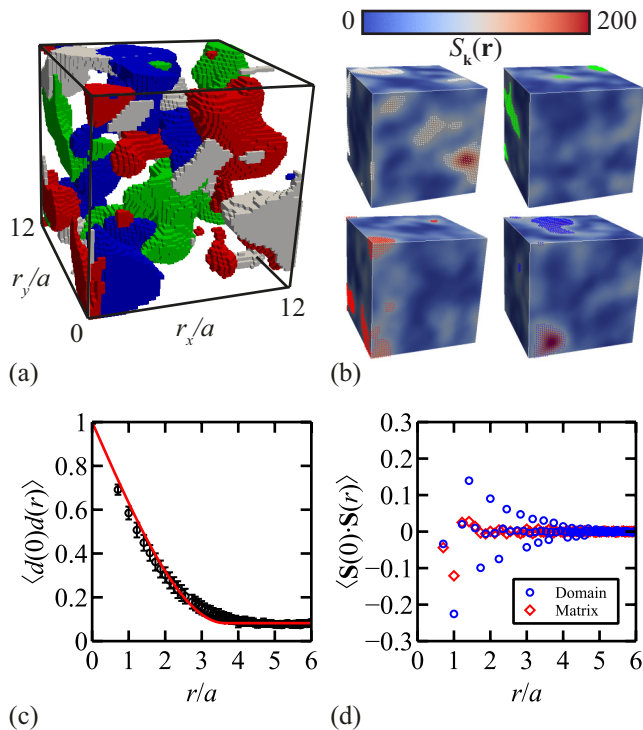
FIG. 4. Magnetic domain structure of MnO at $T = 160$ K obtained as described in the text. In (a), different domains with local periodicity $\mathbf{k} \in \langle \frac{1}{2} \frac{1}{2} \frac{1}{2} \rangle^*$ are shown in different colors. The colored regions show the threshold where $S_{\mathbf{k}}(\mathbf{r}) = 80.6$ [the range of $S_{\mathbf{k}}(\mathbf{r})$ is between approximately 0 and 200]. In (b), the four images show different $\mathbf{k} \in \langle \frac{1}{2} \frac{1}{2} \frac{1}{2} \rangle^*$. The value of $S_{\mathbf{k}}(\mathbf{r})$ in each image is shown using a blue-to-red color map. Colored points indicate the range where $S_{\mathbf{k}}(\mathbf{r}) \geqslant 80.6$, using the same colors as (a). The images in (a) and (b) are shown in the same orientation. (c) Domain-occupancy correlation function described in the text (black circles) and fit to the pair-correlation function for a sphere to extract the average domain radius (red line). Error bars indicate 1 standard deviation. (d) Spin-correlation function for spin pairs within domains (blue circles) and for "matrix" spin pairs that do not belong to any domain (red diamonds). Error bars are smaller than the symbol size in the plot.

sites that are members of a single domain while minimizing the number that are members of more than one domain. We use the threshold value that minimizes the function

$$\chi^2_{\text{domain}} = \sum_{i=1}^{N} \left| \left[\sum_{\mathbf{k}} d_{i,\mathbf{k}} \right]^2 - 1 \right|, \quad (10)$$

where $d_{i,\mathbf{k}} = 1$ if site i is occupied by a domain with propagation vector $\mathbf{k}$ for a given threshold value of $S_{\mathbf{k}}$, and is otherwise zero.

Figure 4(a) shows the regions of a representative RMC configuration in which $S_{\mathbf{k}}(\mathbf{r})$ exceeds the threshold value of 80.6(6) for domain occupancy. These regions contain several continuous and largely nonoverlapping volumes within which a single $\mathbf{k}$ dominates, suggesting that a domainlike structure exists in PM MnO. While the location of such regions within the supercell differs between refinements, as required by the lack of overall symmetry breaking in the PM phase, the

volume occupied by domains was consistently $\sim$35% of the supercell volume. Similar behavior (not shown) is also observed for the J_1-J_2 model. To estimate the length scale over which this structure exists, we define a correlation function of domain occupancies,

$$\langle d(0)d(r) \rangle = \frac{1}{\langle |d_{\mathbf{k}}(0)|^2 \rangle} \sum_{i=1}^{N} \sum_{j=1}^{Z_i(r)} \frac{d_{\mathbf{k},i} d_{\mathbf{k},j}}{Z_i(r)}. \quad (11)$$

The domain correlation function—averaged over all domains and refinements—is shown in Fig. 4(c). This result shows that domains persist over several unit cells—a much longer range than the value of ξ determined by direct analysis of the spin-correlation function. To obtain a quantitative estimate of the domain correlation length, we fit the domain-correlation function using the pair-correlation function for a sphere [47,48],

$$\rho_s(r) = \begin{cases} \rho_{\text{av}} + (1 - \rho_{\text{av}}) \left[\frac{1}{16} \left(\frac{r}{r_0} \right)^3 - \frac{3r}{4r_0} + 1 \right], & r \leqslant 2r_0, \\ \rho_{\text{av}}, & r > 2r_0, \end{cases} \quad (12)$$

where $r_0 = 8.1(1)$ Å is the average domain radius, and $\rho_{\text{av}} = 0.082(2)$ is the limiting value of the domain correlation function at large r. The curvature of $\langle d(0)d(r) \rangle$ is reasonably well approximated by $\rho_s(r)$; the shoulder near $r = 3a$ in the experimental function likely reflects systematic deviations from sphericity. Refinements with a smaller supercell of side length $R = 10a$ yielded a comparable domain radius $r_0 = 7.9(1)$ Å, suggesting that finite-size effects are not significant for these supercell dimensions. Our estimate implies a smaller domain size than the value of $\sim$50 Å reported in Ref. [6]; we note, however, that this value was obtained based on satellite reflections that were not observed in a subsequent experimental study [24]. We also emphasize that these values are dependent on the criteria for assigning spins to domains, as defined in Eqs. (9) and (10). As an independent check on whether spins that belong to a domain are distinguishable from those that do not, we calculate the radial spin-correlation function for (i) pairs of spins that belong to at least one domain of any $\mathbf{k}$ ("domain spins"), and (ii) pairs of spins that do not belong to any domain ("matrix spins"). The calculations were performed using Eq. (7), replacing the normalization by N with the total number of domain spins ($\sim$0.35N) or the total number of matrix spins ($\sim$0.65N), respectively. Results are shown in Fig. 4(d) and indicate that domain-spin correlations are of larger magnitude and range than matrix-spin correlations. Moreover, the domain-spin correlations are much larger at the next-nearest-neighbor distance than the matrix-spin correlations. These results indicate a PM structure that is inhomogeneous on the nanoscale, showing weak and frustrated spin correlations between domains and incipient antiferromagnetic ordering within domains.

IV. CONCLUDING REMARKS

Our study has provided experimental insight into the nature of the cooperative PM phase of MnO. We find a modified AFM-like local order that persists over continuous regions, each associated with one of four symmetry-equivalent modulation vectors $\mathbf{k} \in \langle \frac{1}{2} \frac{1}{2} \frac{1}{2} \rangle^*$ and each spanning several unit cells. The presence of local $\langle \frac{1}{2} \frac{1}{2} \frac{1}{2} \rangle^*$ periodicity provides a natural

explanation for the experimental observation of dispersive (spin-wave-like) excitations in this phase [49]. The clearest difference between local spin correlations in the PM and AFM states is the relief of nearest-neighbor frustration in the former. This effect is analogous to the situation observed in some metallic glasses, where structural units can possess local icosahedral symmetry inconsistent with the long-range structural periodicity of crystalline arrangements [50,51]. Our results are also reminiscent of the proposed coexistence of two different local magnetic structures in the chalcogenide superconductor FeTe, one of which is incompatible with the long-range magnetic order observed in that material [52]. Our observation of nontrivial PM correlations in a weakly frustrated system has implications for the interpretation of spin disorder in other high-temperature superconductors, which have traditionally been assumed to resemble ordered states over short length scales [7].

A second key result of our study is the development of an approach for refining spin configurations against the full 3D neutron-scattering pattern measurable using instruments such as SXD at the ISIS neutron source, containing $>10^6$ data points. This provides a practical model-independent alternative to traditional methods for interpreting diffuse-scattering data [53,54].

[1] R. Moessner and A. P. Ramirez, Phys. Today **59**(2), 24 (2006).

[2] A. P. Ramirez, Annu. Rev. Mater. Sci. **24**, 453 (1994).

[3] S. T. Bramwell, in *Introduction to Frustrated Magnetism*, edited by C. Lacroix, P. Mendels, and F. Mila, Springer Series in Solid-State Sciences Vol. 164 (Springer, Berlin, 2011), Chap. 3.

[4] P. W. Anderson, Phys. Rev. **79**, 705 (1950).

[5] A. T. Boothroyd, P. Babkevich, D. Prabhakaran, and P. G. Freeman, Nature (London) **471**, 341 (2011).

[6] A. Renninger, S. C. Moss, and B. L. Averbach, Phys. Rev. **147**, 418 (1966).

[7] S. Kivelson, I. Bindloss, E. Fradkin, V. Oganesyan, J. Tranquada, A. Kapitulnik, and C. Howald, Rev. Mod. Phys. **75**, 1201 (2003).

[8] A. T. Savici, I. A. Zaliznyak, G. D. Gu, and R. Erwin, Phys. Rev. B **75**, 184443 (2007).

[9] I. A. Zaliznyak and S.-H. Lee, in *Modern Techniques for Characterizing Magnetic Materials* (Springer, New York, 2005), pp. 3–62.

[10] I. A. Blech and B. L. Averbach, Physics **1**, 31 (1964).

[11] T. Fennell, Collection SFN **13**, 04001 (2014).

[12] D. A. Keen and R. L. McGreevy, J. Phys.: Condens. Matter **3**, 7383 (1991).

[13] A. Mellergård, R. L. McGreevy, A. Wannberg, and B. Trostell, J. Phys.: Condens. Matter **10**, 9401 (1998).

[14] R. L. McGreevy, J. Phys.: Condens. Matter **13**, R877 (2001).

[15] M. G. Tucker, D. A. Keen, M. T. Dove, A. L. Goodwin, and Q. Hui, J. Phys.: Condens. Matter **19**, 335218 (2007).

[16] J. A. M. Paddison, J. R. Stewart, and A. L. Goodwin, J. Phys.: Condens. Matter **25**, 454220 (2013).

[17] J. A. M. Paddison, H. Jacobsen, O. A. Petrenko, M. T. Fernández-Díaz, P. P. Deen, and A. L. Goodwin, Science **350**, 179 (2015).

[18] R. W. Tyler, Phys. Rev. **44**, 776 (1933).

[19] G. Pepy, J. Phys. Chem. Solids **35**, 433 (1974).

[20] C. G. Shull and J. S. Smart, Phys. Rev. **76**, 1256 (1949).

[21] W. L. Roth, Phys. Rev. **110**, 1333 (1958).

[22] H. Shaked, J. Faber, and R. L. Hitterman, Phys. Rev. B **38**, 11901 (1988).

[23] A. L. Goodwin, M. G. Tucker, M. T. Dove, and D. A. Keen, Phys. Rev. Lett. **96**, 047209 (2006).

[24] D. Hohlwein, J.-U. Hoffmann, and R. Schneider, Phys. Rev. B **68**, 140408 (2003).

[25] A. Mellergård and R. L. McGreevy, Acta Crystallogr., Sect. A: Found. Adv. **55**, 783 (1999).

[26] T. R. Welberry and T. Proffen, J. Appl. Crystallogr. **31**, 309 (1998).

[27] D. A. Keen, M. J. Gutmann, and C. C. Wilson, J. Appl. Crystallogr. **39**, 714 (2006).

[28] R. I. Bewley, R. S. Eccleston, K. A. McEwen, S. M. Hayden, M. T. Dove, S. M. Bennington, J. R. Treadgold, and R. L. S. Coleman, Physica B (Amsterdam) **385–386**, 1029 (2006).

[29] V. Petricek, M. Dusek, and L. Palatinus, Z. Kristallogr. **229**, 345 (2014).

[30] R. L. McGreevy and L. Pusztai, Mol. Simul. **1**, 359 (1988).

[31] J. A. M. Paddison and A. L. Goodwin, Phys. Rev. Lett. **108**, 017204 (2012).

[32] J. R. Davis and T. J. Hicks, J. Phys. C **9**, L177 (1976).

[33] P. J. Brown, in *International Tables for Crystallography* (Kluwer, Dordrecht, 2004), Vol. C, pp. 454–460.

[34] C. E. Duchon, J. Appl. Meteorol. **18**, 1016 (1979).

[35] B. D. Butler and T. R. Welberry, J. Appl. Crystallogr. **25**, 391 (1992).

[36] R. B. Neder and T. Proffen, *Diffuse Scattering and Defect Structure Simulations: A Cook Book Using the Program DISCUS* (Oxford University Press, Oxford, 2008).

[37] Source code and a manual are available from http://spinvert.chem.ox.ac.uk.

[38] W. Jauch and M. Reehuis, Phys. Rev. B **67**, 184420 (2003).

[39] J. I. Kaplan, J. Chem. Phys. **22**, 1709 (1954).

[40] F. Keffer and W. O'Sullivan, Phys. Rev. **108**, 637 (1957).

[41] J. A. M. Paddison, J. R. Stewart, P. Manuel, P. Courtois, G. J. McIntyre, B. D. Rainford, and A. L. Goodwin, Phys. Rev. Lett. **110**, 267207 (2013).

[42] M. E. Lines, Phys. Rev. **139**, A1304 (1965).

[43] M. E. Lines and E. D. Jones, Phys. Rev. **139**, A1313 (1965).

[44] B. A. Frandsen, M. Brunelli, K. Page, Y. J. Uemura, J. B. Staunton, and S. J. L. Billinge, Phys. Rev. Lett. **116**, 197204 (2016).

[45] L. P. Kadanoff, W. Götze, D. Hamblen, R. Hecht, E. A. S. Lewis, V. V. Palciauskas, M. Rayle, J. Swift, D. Aspnes, and J. Kane, Rev. Mod. Phys. **39**, 395 (1967).

[46] N. Wentzel and S. T. Milner, J. Chem. Phys. **134**, 224504 (2011).

[47] G. Mason, Nature (London) **217**, 733 (1968).

[48] K. Kodama, S. Iikubo, T. Taguchi, and S.-I. Shamoto, Acta Crystallogr., Sect. A: Found. Adv. **62**, 444 (2006).

[49] H. Betsuyaku, Solid State Commun. **26**, 345 (1978).

[50] W. K. Luo, H. W. Sheng, F. M. Alamgir, J. M. Bai, J. H. He, and E. Ma, Phys. Rev. Lett. **92**, 145502 (2004).

[51] H. W. Sheng, W. K. Luo, F. M. Alamgir, J. M. Bai, and E. Ma, Nature (London) **439**, 419 (2006).

[52] I. Zaliznyak, A. T. Savici, M. Lumsden, A. Tsvelik, R. Hu, and C. Petrovic, Proc. Natl. Acad. Sci. USA **112**, 10316 (2015).

[53] T. Fennell, M. Kenzelmann, B. Roessli, M. K. Haas, and R. J. Cava, Phys. Rev. Lett. **109**, 017201 (2012).

[54] P. Manuel, L. C. Chapon, P. G. Radaelli, H. Zheng, and J. F. Mitchell, Phys. Rev. Lett. **103**, 037202 (2009).